Journal of the Optical Society of America B
OPTICAL PHYSICS

Truly achromatic optical metasurfaces: a filter circuit theory-based design

JIERONG CHENG AND HOSSEIN MOSALLAEI*

Department of Electrical and Computer Engineering, Northeastern University, 360 Huntington Ave., Boston, Massachusetts 02115, USA
**Corresponding author: hosseinm@ece.neu.edu*

Received 13 July 2015; revised 19 August 2015; accepted 22 August 2015; posted 24 August 2015 (Doc. ID 245732); published 14 September 2015

We propose truly achromatic metasurfaces at midinfrared and visible spectra using plasmonic and all-dielectric concepts, respectively. The constituting layered elements, with each layer being a capacitive or an inductive structure, behave like low-pass circuit filters with almost linear phase response over the designed spectrum. This allows successful broadband operation. The plasmonic layered elements are limited to work around 50 THz due to the appearance of a plasmonic resonance feature at higher frequencies. On the other hand, the all-dielectric concept can be designed up to the visible range with negligible material dispersion. Design procedures and working principles are fully detailed. Two types of metasurfaces patterned by plasmonic and all-dielectric elements are carefully designed and numerically simulated around 50 and 600 THz, respectively. Chromatic aberration is successfully avoided. The plasmonic metasurface operates well in 5.5–7.5 μm, and the all-dielectric case has the desired performance over almost the entire visible band.

OCIS codes: (160.3918) Metamaterials; (050.5080) Phase shift; (260.2030) Dispersion.

http://dx.doi.org/10.1364/JOSAB.32.002115

1. INTRODUCTION

Metasurfaces have been of great interest for wavefront engineering by providing a space-variant phase shift from constituting subwavelength inclusions [1–3]. Different from the traditional realization based on the propagation accumulation, the phase shift here is generated abruptly within an ultrathin layer due to the resonant interaction between the incoming light and the inclusions. Such resonance provides large flexibility to reconfigure the amplitude, phase, and polarization responses of the scattered light, realized by manipulating the element material, geometry, period, and orientation. A variety of innovative functionalities have been demonstrated ranging from microwave to visible ranges, including anomalous reflection and refraction [4,5], beaming and focusing [6,7], information processing [8,9], vortex beam generation [10], quarter and half-wave plate [11], phase holograms [12], and so forth.

At the same time, it is the resonant nature of the phase shift that brings a common limitation for many applications of such kind of metasurfaces, which is the single-frequency or narrowband operation (around 5% or even less). Although the bandwidth can be increased by cascading resonant elements [13,14], the phase profile across the entire surface is frequency-dependent and changes either rapidly or slowly depending on the quality factor of the element resonance, hampering widespread applications.

Achromatic wavefront shaping is highly desirable for numerous applications, including communication systems, sensing, imaging, and energy harvesting. Several techniques have been proposed to address the issue of narrow bandwidth. One model is to change the multiband design into broadband design by merging multiple closely positioned resonances [15,16], where complex element structures are usually needed. Another type of broadband metasurfaces can maintain the performance fairly well within a certain frequency range, although these surfaces are designed to operate at one selected frequency [17,18]. Such bandwidth is uncontrollable, and the performance is still frequency-dependent. For example, the bending angle of the anomalous beam is different because the frequency changes in the V-shaped nanoantennas array [18]. The focal length and the spot intensity are varying with frequency in the broadband flat mirrors [17]. Thus, such wideband operation suffers from chromatic aberration.

Geometric metasurfaces made of a single layer of dipole antennas have been reported recently for dispersionless wavefront shaping [19–21]. The phase gradient of the cross polarization does not depend on the dispersion of the dipole antennas but depends on the orientation of the dipoles when the surface is illuminated by the circularly polarized wave only. The efficiency is inherently limited due to the cross-polarization working scheme, though.

Truly broadband operation requires a constant group delay profile (i.e., a linear phase delay profile) as group delay is the rate of phase variation over frequency. Otherwise, changing the frequency will change the phase response of each element

undesirably, and the performance will be degraded. Recently, a broadband true-time-delay microwave lens was theoretically and experimentally demonstrated based on the filter circuit theory. It is composed of subwavelength unit cells of closely spaced capacitive and inductive layers [22,23]. Each layer of the unit cell is a nonresonant structure, and the proper cascading of the layers in the propagation direction forms a spatial filter with a designed bandpass or low-pass response. Within the operation band, the phase response is linear and the group delay is constant, enabling the truly dispersionless broadband operation.

In this work, we theoretically extend this mechanism from microwave to *infrared* and *visible* ranges. Material dispersion of the metallic layers prohibits us to directly scale up the microwave design, and a comprehensive design study must be performed. Also, the plasmonic effect poses limitations that such broadband metasurface can work only up to the midinfrared range. The metallic patches and wires begin to resonate at higher frequencies, and they cannot be treated as pure capacitors or inductors. We also investigate the concept of all-dielectric metasurfaces made of high/low-index dielectric layered unit cells functioning at the visible frequency range.

Specifically, the design principle of the broadband phase shift element is generally stated based on the filter circuit theory. Then, such element is realized, respectively, by layered plasmonic patches separated by dielectric spacers at the midinfrared range and by all-dielectric layers with alternating high and low refractive indices at the visible range. Two types of metasurface lenses without chromatic aberration are designed and numerically demonstrated at 40 to 55 THz (~5.5–7.5 μm) and 450 to 750 THz (covering almost the entire visible band) using plasmonic and all-dielectric layered concepts, respectively. To the best of our knowledge, these will be the first truly wideband metasurfaces designed at a high-frequency range. Also, wideband beam scanning performance is demonstrated due to the deep subwavelength thickness and the element period.

2. PHASE MANIPULATION BASED ON FILTER THEORY

Generally, the truly dispersionless broadband operation requires a constant group delay (i.e., a linear phase delay) through the metasurface element over frequency. Such characterization can be found in the passband of a microwave filter circuit made of lumped capacitors and inductors [24]. We design the metasurface of Fig. 1(a) with each element behaving like a low-pass filter working in infrared to visible frequency ranges.

The metasurface is composed of ultrathin layered elements in Figs. 1(b) and 1(c) with subwavelength lattice constant to physically approach the constant group delay response of a low-pass filter. The element in Fig. 1(b) is composed of three layers of plasmonic patches separated by two dielectric spacers, while in the element of Fig. 1(c), plasmonic patches are replaced by high-index dielectric thin layers. The equivalent circuit for such two types of layered elements is shown in Fig. 1(d), where the dielectric spacer has a π-shape transmission line model, and the plasmonic patches and high-index dielectric slices are represented by shunt capacitors. Such circuits can be simply transformed to a ladder network of five-order low-pass

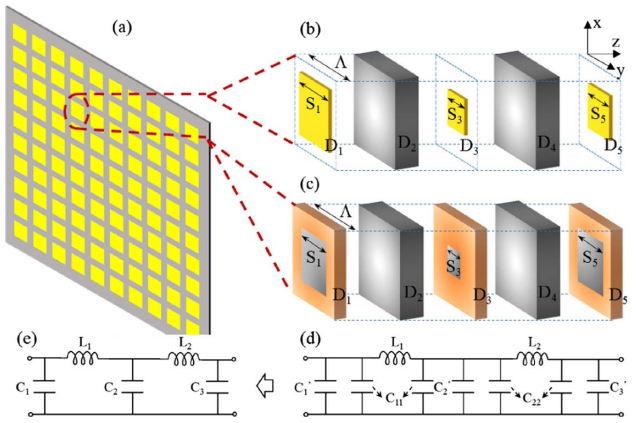

Fig. 1. (a) Topology of the metasurface for broadband operation. (b) Dispersionless metasurface element made of plasmonic patches and dielectric spacers cascaded sequentially. Patch size is variable for different phase responses. (c) Dispersionless metasurface element made of high and low index dielectric layers cascaded sequentially. The high index is variable by mixing two types of materials with different filling factors. (d) Equivalent circuit model for elements in (b) and (c), which is simplified as a five-order low-pass filter in (e).

filters, as shown in Fig. 1(e). Thus, it is possible to design the layered elements with constant group delay over frequency and different group delay along the surface, enabling the wideband application of the metasurface.

Due to the distributed feature of the elements, one should expect the variation of the group delay within the passband. Nevertheless, as long as the dielectric slabs have deep-subwavelength thickness, and the plasmonic patches are far away from resonances, the frequency dependence of the equivalent inductance and capacitance is fairly weak over a wide frequency range.

Given the cut-off frequency of the filter, we map the circuit parameters of Fig. 1(e) to the geometric parameters of the elements in Figs. 1(b) and 1(c). Group delay and phase response of such elements are then numerically analyzed and optimized in a periodic environment. By changing the cut-off frequency of the circuit, one will determine different geometric parameters, leading to different group delays. A data set is established for the mapping between the geometry of the element and the desired group delay, which will guide us in the design of various broadband wave manipulation. Design examples of metasurface elements will be detailed next.

3. PLASMONIC LAYERED ELEMENTS

The values of lumped elements in Fig. 1(e) can be easily found [25] once the filter type (i.e., Butterworth and Chebyshev), the cut-off frequency f_{cut}, and the source and load impedances are determined. The series inductance, L_1 and L_2, determines the thickness, D_2 and D_4, of the two dielectric spacer layers by [26]

$$D_{2,4} = a \sin\left(\frac{\omega_0 L_{1,2}}{\eta}\right)/\beta. \quad (1)$$

Here, the material of the spacer layer and the background is chosen as SiO_2 with permittivity of 2.25. η, ω_0, and β are the wave impedance, angular frequency, and wave vector, respectively, at desired center frequency f_0. D_2 and D_4 are then

fixed for different group delay elements to keep the uniform thickness over the surface. C_{11} and C_{22} are known based on these slab thicknesses. Values for C_1', C_2', and C_3' can be derived accordingly. Given a deep-subwavelength period Λ, C_1', C_2', and C_3' can be converted to plasmonic patch size S_1, S_3, and S_5, with ultrathin thickness D_1, D_3, and D_5, which is detailed as follows.

When the period Λ is much smaller than the wavelength, and the metallic patches are perfect electrical conductors (PEC), which is the case at microwave frequency, they act as pure capacitors between the adjacent patch edges for the orthogonally incoming light. The relation between the capacitance and the geometrical size of the patch can be found in [27]. As the frequency increases, the permittivity of metal should be described by the Drude model, and the finite thickness, even though in the deep subwavelength scale, also plays a role in the optical response. Thus, the mapping between the capacitance and the geometrical parameters should be modified. Here, finite-difference time-domain (FDTD) simulations are used to capture the effective capacitance of the periodic metallic patches with different patch size S.

The plasmonic patch is made of Au with the permittivity modeled by the Drude model [28]. It is periodically patterned within the x–y plane and embedded in the uniform background with relative permittivity of 2.25. To obtain the equivalent capacitance, the transmission and reflection spectrums of periodic patches with desired patch size are numerically obtained in FDTD with plane wave excitation propagating along z and polarized along x. Then, the theoretical transmission and reflection of a pure capacitor are calculated from the circuit theory and fitted to the numerical results to obtain the optimum equivalent capacitance. Figure 2(a) shows a specific example working around 50 THz. The period of the patch is $\lambda_0/6$, where λ_0 is the free-space wavelength at 50 THz. The patch size is 480 nm with the thickness of $\lambda_0/150$. The numerical responses (solid lines) and the theoretical results (dots) agree perfectly within a large bandwidth centered at 50 THz, when the equivalent capacitance for such periodic patch is given as $C = 3.71$ aF.

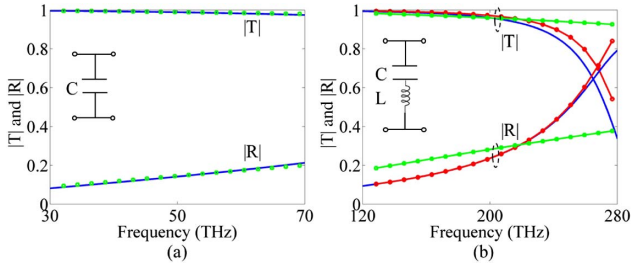

Fig. 2. (a) Transmission and reflection spectrums of periodic Au patches around 50 THz with period of 1 μm, patch size of 480 nm, and thickness of 40 nm. Solid blue lines: FDTD numerical results; green dots: theoretical fitting using a pure capacitor with $C = 3.71$ aF. (b) Transmission and reflection spectrums around 200 THz of periodic Au patches with period of 250 nm, patch size of 120 nm, and thickness of 10 nm. Solid blue lines: FDTD numerical results; green dotted line: theoretical fitting using a pure capacitor with $C = 1.86$ aF; red dotted lines: theoretical fitting using series capacitor and inductor with $C = 0.83$ aF and $L = 0.351$ pH.

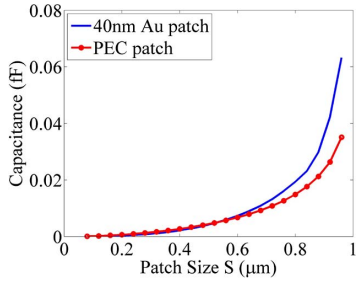

Fig. 3. Correlation between the plasmonic patch size and the capacitance. Blue solid line: capacitance of 40 nm thick periodic Au patch with period of 1 μm obtained numerically around 50 THz, where the permittivity is a Drude model. Red dashed line: theoretical capacitance of PEC patch with the same period. At midinfrared range, in order to obtain the same capacitance, one should use smaller Au patch size compared with the PEC.

To further detect the upper-frequency limit when the Au patch behaves as a capacitor, we then move the working frequency to the near-infrared range around 200 THz. The period is still kept as $\lambda_0/6$ and the thickness to be $\lambda_0/25$, with λ_0 being the wavelength at 200 THz. The patch size is scaled accordingly to 120 nm. The numerical transmission and reflection spectrums are given as the blue solid lines in Fig. 2(b). The optimized fitting results of the green dot lines show large deviation by considering the patch as a pure capacitor. On the other hand, the response of a capacitor and an inductor in series gives satisfactory agreement with the numerical results as the red dotted lines, when $C = 0.83$ aF and $L = 0.351$ pH. This means that the patch itself is a plasmonic resonant structure around 200 THz and cannot be modeled by a pure capacitor. Thus, we limit the dispersionless plasmonic element design to the midinfrared range around 50 THz.

Figure 3 shows the relation between the capacitance and the patch size using the same period and patch thickness in Fig. 2(a) from 30 to 70 THz. The mapping relation for patches made of PEC is also given as a comparison. As can be seen, to achieve the same capacitance, the required patch size is smaller for the Au patch compared with the PEC patch, which means one cannot directly scale the microwave design up to the midinfrared range. The plasmonic patch should be shrunken appropriately to achieve good performance.

Next, the dispersionless elements are designed for different group delays. The element is made to mimic the five-order Chebyshev 0.1 dB low-pass filter. The relative permittivity of the background and the dielectric layers is 2.25. The dielectric layer thickness, D_2 and D_4, is calculated to be 540 nm when $f_{cut} = 90$ THz and $f_0 = 50$ THz. Then, four different periodic elements are shown with cut-off frequency of $f_{cut} = \infty$, 80, 60, and 45 THz. C_1', C_2', and C_3' are derived for each case, and the patch sizes S_1, S_3, and S_5 are determined based on Fig. 3. The total thickness of the five-layer element is 1.2 μm with a transverse period of 1 μm. The transmission amplitude, phase, and group delay of each periodic element are detailed in Fig. 4. It is worth noting that the realized cut-off frequencies for the elements are different from the designed ones. This is due to the fixed dielectric layer thickness, which cannot provide the ideal inductance for all the filter

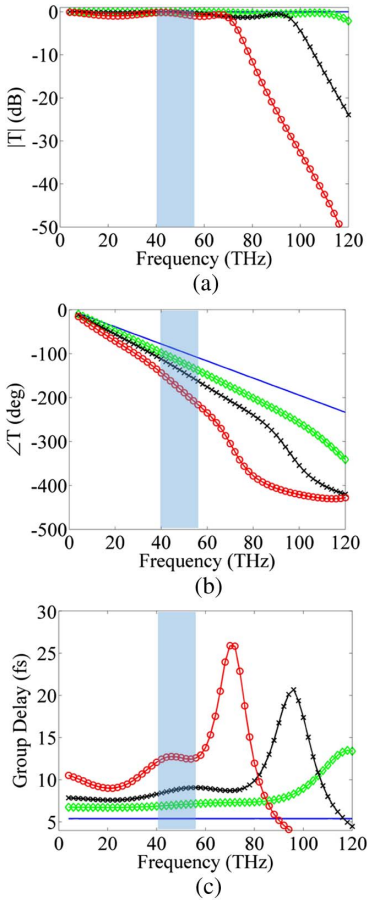

Fig. 4. (a) Transmission amplitudes, (b) phases, and (c) group delays of plasmonic elements with designed cut-off frequencies of ∞, 80, 60, and 45 THz (blue solid line, green diamond line, black cross line, and red circle line, respectively), realized by choosing different patch sizes of S_1, S_3, and S_5. Within the shaded frequency range [40 55] THz, all the elements can be viewed as dispersionless.

responses. Nevertheless, within the shaded frequency range [40 55] THz, group delays can still be viewed as constant approximately for all the elements. Linear phase response and high transmission efficiency are achieved at the same time.

The maximum group delay variation among the elements in Fig. 4(c) is 7.3 fs within the [40 55] THz band. The smallest group delay is the case when all the plasmonic patches are absent, corresponding to the cut-off frequency of ∞. As the cut-off frequency moves close to 50 THz, the group delay value increases. Meanwhile, the variation of the group delay increases due to the deviation from the ideal filter components. Thus, there is a trade-off relation between the available group delay range and the operation bandwidth. One way to further increase the group delay range without sacrificing the bandwidth is to use higher-order filter elements with more layers, which will increase the fabrication complexity.

4. ALL-DIELECTRIC LAYERED ELEMENTS

Plasmonic layered elements are limited to work at the midinfrared range due to the resonant nature of the patches at higher frequencies. To overcome such limitation, the patch can be replaced by an ultrathin layer of high-index dielectric slab. The equivalent circuit for such a slab is simplified into a shunt capacitor. Thus, the all-dielectric layered element in Fig. 1(c) is made of five layers of dielectric slabs, with the second and the fourth layers to be the low-index SiO_2 slabs to provide the series inductors, and the remaining three high-index layers to provide the parallel capacitors like the plasmonic patches. At the mid-infrared range, plasmonic patch size is a tunable parameter to realize different group delays. Here, the equivalent index of the slab can be changed by mixing two types of dielectrics for the realization of different group delays. We mix Si (relative permittivity of 12.25) and SiO_2 within a subwavelength period to obtain different indices and different capacitances for the first, third, and fifth layers. The thickness of each slab layer is still fixed considering the feasibility of fabrication.

The design principle of such element is the same as the plasmonic case, except that the mapping relation is from C_1', C_2', and C_3' to the equivalent indices and finally to the filling factors of SiO_2 in Si slab for the first, third, and fifth layers. Next, a sample element is designed to work around 500 THz with cut-off frequency of 800 THz. The second and fourth layers are SiO_2 slabs with thickness of 18 nm. The thickness of the high-index layer can be arbitrarily small theoretically. But unrealistically high index is needed if the slab is too thin. Considering the largest available permittivity of 12.25, the thickness of the first, third, and fifth layers is given as $D_1 = 15$ nm, $D_3 = 25$ nm, and $D_5 = 15$ nm, respectively. Thus, the total thickness of such element is 91 nm. The relative permittivity of each layer ($\varepsilon_{1,3,5}$) is related to the desired capacitance (C_1', C_2', C_3') by the following equation:

$$-j\frac{\eta_0}{\sqrt{\varepsilon_{1,3,5}}}\cot\left(\sqrt{\varepsilon_{1,3,5}}\beta_0 D_{1,3,5}\right) = \frac{1}{j\omega_0 C'_{1,2,3}}, \quad (2)$$

where β_0 and η_0 are for the free-space case at the center frequency ω_0. The required relative permittivity for each layer in this element is calculated to be 6.32, 6.47, and 6.32. The mixing ratio of SiO_2 and Si to realize the permittivity in each layer can be determined by the effective medium theory (EMT) [28] if the period is in subwavelength scale.

One should note that the choice of the period can be arbitrarily small and will be limited by the fabrication ability. Each layer is a nonresonant structure. The interaction of the cascading layers provides the desired response, which does not depend on the period. Here, we use the period of $\Lambda = 50$ nm ($\lambda_0/12$ at 500 THz) in order to ensure that EMT works perfectly to determine the indices of the first, third, and fifth layers. The filling factor of the SiO_2 inside the Si slab is defined as S/Λ, where S is the side length of the SiO_2 square, as shown in Fig. 1(c). The effective permittivity of the designed slab follows [29]

$$\sqrt{\varepsilon_{\text{eff}}} = \left(1 - \frac{S^2}{\Lambda^2}\right)\sqrt{\varepsilon_{\text{Si}}} + \frac{S^2}{\Lambda^2}\sqrt{\varepsilon_{\text{SiO}_2}}. \quad (3)$$

This is verified by the FDTD simulations for the first and fifth layers in Fig. 5(a) and for the third layer in Fig. 5(b), showing that the effective permittivity does not depend on the thickness of the slab.

Then, the filling factors of SiO_2 in the first, third, and fifth layers are obtained as 0.69, 0.70, and 0.69 to realize the permittivities of 6.32, 6.47, and 6.32. Finally, this five-layer

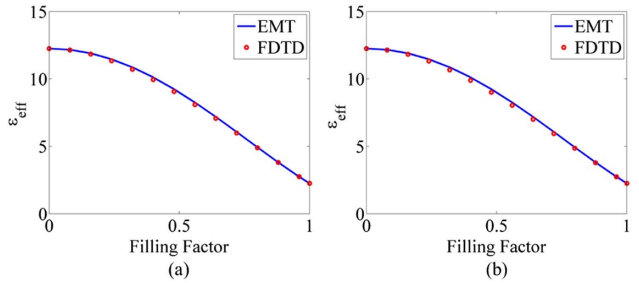

Fig. 5. Verification of the validity of effective medium theory by numerical FDTD simulations (a) for mixing layer thickness of 15 nm, corresponding to the first and fifth layers, and (b) for layer thickness of 25 nm in the third layer.

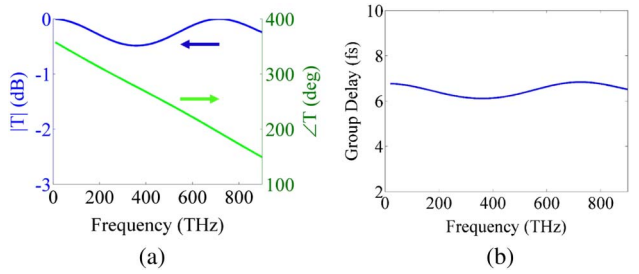

Fig. 6. Design example of a filter element made of all-dielectric materials. The element has five layers along the z direction and period of 50 nm along the x and y directions. Thickness of each layer: 15, 18, 25, 18, 15 nm. Relative permittivity of each layer: 6.32, 2.25, 6.47, 2.25, 6.32. The second and fourth layers are fixed as SiO_2. Other layers are realized by mixing SiO_2 and Si with filling factors of 0.69, 0.70, and 0.69. Permittivities of Si and SiO_2 are assumed to be dispersionless within the design range.

element has the transmission response in Fig. 6. Proper choice of the frequency range leads to the group delay variation within a very small range, for example, [400 600] THz. Different group delays can be achieved by properly modifying the filling factors of the high-index layers.

5. METASURFACE LENSES WITH BROADBAND OPERATION

Broadband metasurface lenses with negligible frequency dispersion are designed to work at midinfrared and visible ranges using the two types of filter elements analyzed in the previous section.

To validate the principle of broadband operation, a small flat lens working around 50 THz is designed, composed of 11 plasmonic layered elements along x and uniform elements along y, as indicated by Fig. 7(a). These 11 elements have different group delays in the periodic environment, and the configuration of these elements forms the desired group delay profile for a lens in Fig. 7(b). The ideal group delay profile is shown as the solid line when $f/D = 0.98$. Here f is the focal length and $D = 11$ μm is the dimension of the lens. The maximum group delay difference between element a and f is 5.52 fs, which can be realized using the five-order filter elements.

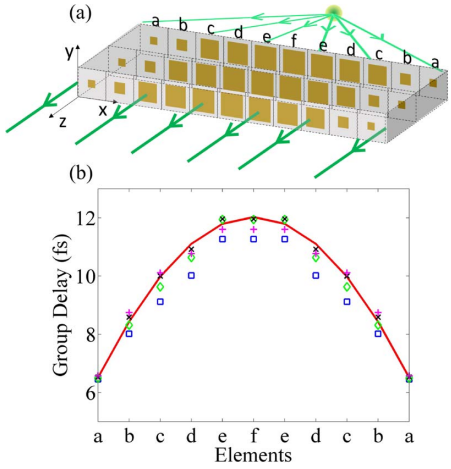

Fig. 7. (a) Layout of the collimating metasurface lens with total thickness of 1.2 μm. (b) Group delay profile for the lens composed of 11 elements along x and uniform along y with $f/D = 0.98$ and $D = 11$ μm. Red solid line: ideal group delay for each element; blue squares, green diamonds, black crosses, and magenta pluses are the realized group delays at 40, 45, 50, and 55 THz.

Then, six types of metallic layered elements are needed to provide the desired group delays based on the filter design procedure with different cut-off frequencies. The period of the element is $\Lambda = 1$ μm. The total thickness of the five layers is 1.2 μm with $D_2 = D_4 = 540$ nm and $D_1 = D_3 = D_5 = 40$ nm. The Au patch size, S_1, S_3, and S_5, is varied from element to element in order to realize different cut-off frequencies and different group delays. Detailed information of the transmission amplitude, phase and group delay for each periodic element is illustrated in Fig. 8 from 40 to 55 THz. The transmission amplitude keeps above −1 dB for all the elements within this frequency band, meaning an efficiency of larger than 80%. The transmission phase is linearly decreasing with frequency. All the group delays have variations of less than 5%. In order to make a clear comparison, the group delay for each lens element at four different frequencies from 40 to 55 THz (~5.5–7.5 μm) is added on top of the ideal values in Fig. 7(b). The realized group delays show pretty good coincidence to the ideal values at 45, 50, and 55 THz, while a relatively large deviation is seen at 40 THz.

Until now, separate analysis of each periodic element is done. Then, we numerically simulate the whole metasurface in FDTD by putting them together and considering all the interactions among different elements. A point source is placed at the designed focal point of the lens with polarization along x. Periodic boundary condition is used in the y direction, and perfectly matched layers are added in the x and z directions. The near-field phase front evolution through the metasurface is shown in Fig. 9 at different frequencies. The circular phase front is collimated into a plane wave after the lens at all the tested frequencies with the same focal length, validating the wideband operation with a bandwidth larger than 30%. Despite the relatively small size of the metasurface, it still functions successfully. This should be attributed to the subwavelength element size, which provides enough resolution of the transverse phase profile.

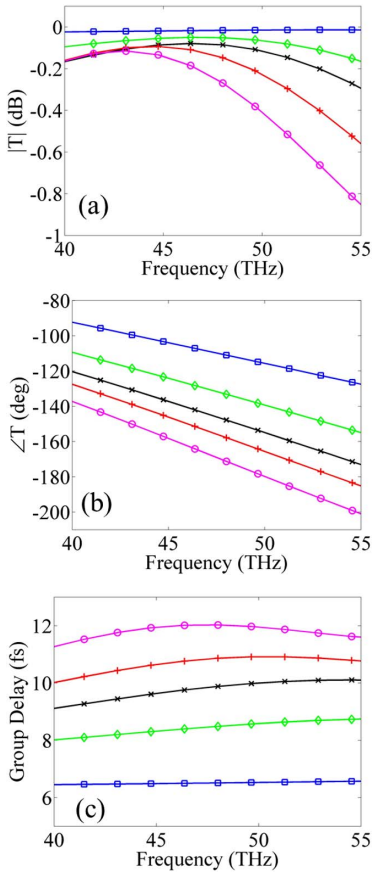

Fig. 8. (a) Transmission amplitudes, (b) phases, and (c) group delays over frequency for all the lens elements from a to f in a periodic environment. Elements e and f are the same here due to the tiny difference between them. Blue squares: element a; green diamonds: element b; black crosses: element c; red pluses: element d; magenta circles: elements e and f.

Although the periodic elements are analyzed under normal excitation, their wideband performance is kept well for the oblique incidence in Fig. 10. The subwavelength element size and small thickness make the whole lens not sensitive to the incident angle. To further utilize this advantage, the collimation direction can be scanned by moving the excitation source along the focal plane, as shown in Fig. 10. The point source is now located at $x = 3$ μm along the focal plane. The time

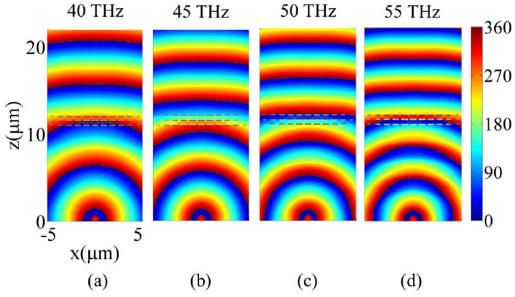

Fig. 9. Phase front evolution of a point source before and after the metasurface composed of plasmonic elements, showing the same collimation performance from 40 to 55 THz. Dashed lines are the cross section of the plasmonic patches.

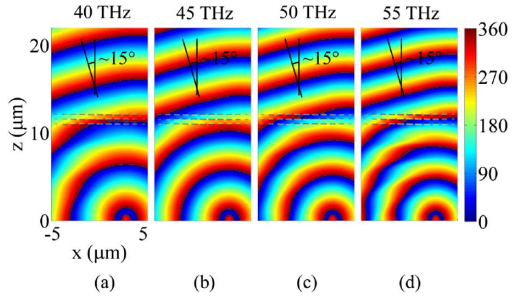

Fig. 10. Collimation direction is scanned to 15° by moving the point source to $x = 3$ μm along the focal plane from 40 to 55 THz using the plasmonic metasurface.

delays after the 11 lens elements are not uniform but decreasing linearly from the $-x$ to $+x$ direction, thus leading to a scanned collimation beam. The time delay difference between adjacent elements after the lens is calculated to be 1.25 fs, which corresponds to the bending angle of 15.5°. And the simulated results are consistent with the expectation over the designed bandwidth. By moving the source further away from the center along x, the beam can be scanned to a wider angular range.

To realize achromatic operation at the visible range, a focusing metasurface lens made of all-dielectric layered elements is designed and analyzed numerically. The layout is in the x–y plane with 19 elements along the x and periodic along the y direction. The elements have the same parameters as the example in Fig. 6, except for the fractions of SiO_2 in the Si layers. By tuning the filling fractions in the first, third, and fifth layers of the element, they provide the desired group delay profile for a lens with $f/D = 1$ and $D = 0.95$ μm. The total thickness of this metasurface is 91 nm, which is less than $\lambda_0/5$ considering the center frequency of 600 THz. The uniform plane wave is launched into this metasurface along the z direction with the electric field polarized along x. The focusing phenomenon is numerically analyzed in Fig. 11 from 450 to 750 THz with 50 THz steps. Intensity of the electric field is plotted after normalization. The focal point is marked in each frequency case. The focal length does not change much across the whole visible range. Thus, the chromatic aberration is successfully minimized. In addition, because we are modeling a finite size metasurface, obviously the larger the frequency, the narrower the spot size, as the electrical size of the structure is larger at a higher frequency.

For either the plasmonic or the all-dielectric elements designed here, the available phase range is limited within

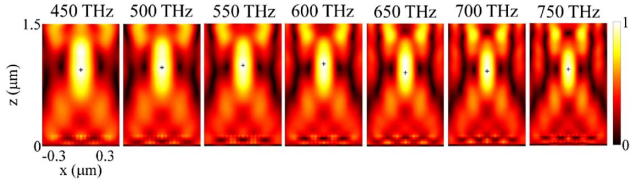

Fig. 11. Beam focusing through the all-dielectric layered metasurface from 450 to 750 THz with 50 THz steps. The transverse dimension along x is 0.95 μm, and the total thickness is 91 nm. The focal point is marked by a black plus sign in each frequency, which shows extremely minor chromatic aberration.

the operation band when the cut-off frequency is changed. If one intends to scan the beam to a larger angle or focus the beam with shorter focal length while keeping the wide bandwidth, it would be desirable to have a dynamic phase range of 360° or larger within the working bandwidth. This can be done by adding more layers based on the higher-order filter circuit model.

Finally, to comment on the fabrication possibility of the two metasurfaces, although five layers are used, the thickness of each layer is very small, which is not a challenge for deposition, lithography, and patterning layer by layer. The plasmonic metasurface has the lattice period of 1 μm with the patterning resolution above 20 nm, which is well within the current nanofabrication capability. The dielectric metasurface can be of some challenge for fabrication because it has a small lattice size of 50 nm. However, some of the approaches such as patterned dielectrics for transformation optics might be considered [30]. Note that the working principle of the proposed metasurfaces does not rely on the element period and one can scale it up.

6. SUMMARY

Achromatic metasurfaces for light management (bending and lensing) in midinfrared and visible spectra are introduced. The structures are thin and function upon the filter circuit theory where almost-constant group delays are realized. Plasmonic and all-dielectric cases are investigated. Plasmonic configuration is designed for operation in the infrared range with plasmonic patches gap coupling behaving as shunt capacitors and dielectric spacers as the series inductors. All-dielectric design works at the visible range with the high-index dielectric slice as the shunt capacitor and the low-index dielectric slice as the series inductor. Collimating, scanning, and focusing metasurfaces are studied. The broadband performance is verified with negligible chromatic aberration for the plasmonic case from about 5.5–7.5 μm and for all-dielectric case in almost the entire visible band. This will be the first demonstration of a truly achromatic metasurface in the optical range. We need to stress that this is a broadband design and not a multiband behavior. Besides the applications presented here, other types of light management devices can be inspired by the achromatic concept proposed in this paper.

Funding. Air Force Office of Scientific Research (AFOSR) (#FA9550-14-1-0349).

REFERENCES

1. N. Yu and F. Capasso, "Flat optics with designer metasurfaces," Nat. Mater. **13**, 139–150 (2014).
2. N. Meinzer, W. L. Barnes, and I. R. Hooper, "Plasmonic meta-atoms and metasurfaces," Nat. Photonics **8**, 889–898 (2014).
3. A. E. Minovich, A. E. Miroshnichenko, A. Y. Bykov, T. V. Murzina, D. N. Neshev, and Y. S. Kivshar, "Functional and nonlinear optical metasurfaces," Laser Photon. Rev. **9**, 195–213 (2015).
4. N. Yu, P. Genevet, M. A. Kats, F. Aieta, J.-P. Tetienne, F. Capasso, and Z. Gaburro, "Light propagation with phase discontinuities: generalized laws of reflection and refraction," Science **334**, 333–337 (2011).
5. A. V. Kildishev, A. Boltasseva, and V. M. Shalaev, "Planar photonics with metasurfaces," Science **339**, 1232009 (2013).
6. J. Cheng and H. Mosallaei, "Optical metasurfaces for beam scanning in space," Opt. Lett. **39**, 2719–2722 (2014).
7. J. Cheng, D. Ansari-Oghol-Beig, and H. Mosallaei, "Wave manipulation with designer dielectric metasurfaces," Opt. Lett. **39**, 6285–6288 (2014).
8. M. Farmahini-Farahani, J. R. Cheng, and H. Mosallaei, "Metasurfaces nanoantennas for light processing," J. Opt. Soc. Am. B **30**, 2365–2370 (2013).
9. A. Silva, F. Monticone, G. Castaldi, V. Galdi, A. Alù, and N. Engheta, "Performing mathematical operations with metamaterials," Science **343**, 160–163 (2014).
10. Y. Yang, W. Wang, P. Moitra, I. I. Kravchenko, D. P. Briggs, and J. Valentine, "Dielectric meta-reflectarray for broadband linear polarization conversion and optical vortex generation," Nano Lett. **14**, 1394–1399 (2014).
11. Y. Zhao and A. Alù, "Tailoring the dispersion of plasmonic nanorods to realize broadband optical meta-waveplates," Nano Lett. **13**, 1086–1091 (2013).
12. S. Larouche, Y.-J. Tsai, T. Tyler, N. M. Jokerst, and D. R. Smith, "Infrared metamaterial phase holograms," Nat. Mater. **11**, 450–454 (2012).
13. B. Memarzadeh and H. Mosallaei, "Layered plasmonic tripods: an infrared frequency selective surface nanofileter," J. Opt. Soc. Am. B **29**, 2347–2351 (2012).
14. M. Farmahini-Farahani and H. Mosallaei, "A plasmonic MIM frequency diplexer," IEEE Trans. Nanotechnol. **12**, 361–367 (2013).
15. F. Ding, Y. Cui, X. Ge, Y. Jin, and S. He, "Ultra-broadband microwave metamaterial absorber," Appl. Phys. Lett. **100**, 103506 (2012).
16. Y. Cui, J. Xu, K. Hung Fung, Y. Jin, A. Kumar, S. He, and N. X. Fang, "A thin film broadband absorber based on multi-sized nanoantennas," Appl. Phys. Lett. **99**, 253101 (2011).
17. A. Pors, M. G. Nielsen, R. L. Eriksen, and S. I. Bozhevolnyi, "Broadband focusing flat mirrors based on plasmonic gradient metasurfaces," Nano Lett. **13**, 829–834 (2013).
18. X. J. Ni, N. K. Emani, A. V. Kildishev, A. Boltasseva, and V. M. Shalaev, "Broadband light bending with plasmonic nanoantennas," Science **335**, 427 (2012).
19. E. Hasman, V. Kleiner, G. Biener, and A. Niv, "Polarization dependent focusing lens by use of quantized Pancharatnam-Berry phase diffractive optics," Appl. Phys. Lett. **82**, 328–330 (2003).
20. L. Huang, X. Chen, H. Mühlenbernd, G. Li, B. Bai, Q. Tan, G. Jin, T. Zentgraf, and S. Zhang, "Dispersionless phase discontinuities for controlling light propagation," Nano Lett. **12**, 5750–5755 (2012).
21. D. Lin, P. Fan, E. Hasman, and M. L. Brongersma, "Dielectric gradient metasurface optical elements," Science **345**, 298–302 (2014).
22. L. Meng, M. A. Al-Joumayly, and N. Behdad, "Broadband true-time-delay microwave lenses based on miniaturized element frequency selective surfaces," IEEE Trans. Antennas Propag. **61**, 1166–1179 (2013).
23. L. Meng and N. Behdad, "Wideband true-time-delay microwave lenses based on metallo-dielectric and all-dielectric lowpass frequency selective surfaces," IEEE Trans. Antennas Propag. **61**, 4109–4119 (2013).
24. D. M. Pozar, *Microwave Engineering* (Wiley, 2005).
25. J. B. Hagen, *Radio-Frequency Electronics: Circuits and Applications* (Cambridge University, 1996).
26. S. J. Orfanidis, *Electromagnetic Waves and Antennas* (Rutgers University, 2008).
27. O. Luukkonen, C. Simovski, G. Granet, G. Goussetis, D. Lioubtchenko, A. V. Raisanen, and S. A. Tretyakov, "Simple and accurate analytical model of planar grids and high-impedance surfaces, comprising metal strips or patches," IEEE Trans. Antennas Propag. **56**, 1624–1632 (2008).
28. M. A. Ordal, R. J. Bell, R. W. Alexander, L. L. Long, and M. R. Querry, "Optical properties of fourteen metals in the infrared and far infrared: Al, Co, Cu, Au, Fe, Pb, Mo, Ni, Pd, Pt, Ag, Ti, V, and W," Appl. Opt. **24**, 4493–4499 (1985).
29. R. Brauer and O. Bryngdahl, "Design of antireflection gratings with approximate and rigorous methods," Appl. Opt. **33**, 7875–7882 (1994).
30. J. Valentine, J. Li, T. Zentgraf, G. Bartal, and X. Zhang, "An optical cloak made of dielectrics," Nat. Mater. **8**, 568–571 (2009).